Micromagnetic determination of the FORC response of paleomagnetically significant magnetite assemblages

Lesleis Nagy[1], Roberto Moreno Ortega[2,3], Adrian R. Muxworthy[4,5], Wyn Williams[2], Greig A. Paterson[1], Lisa Tauxe[6], and Miguel A. Valdez-Grijalva[7]

[1]Department of Earth, Ocean and Ecological Sciences, University of Liverpool, Liverpool, UK.
[2]School of GeoSciences, University of Edinburgh, Edinburgh, UK
[3]CONICET, Instituto de Física Enrique Gaviola (IFEG), Córdoba, Argentina
[4]Department of Earth Science and Engineering, Imperial College London, London, UK.
[5]Department of Earth Sciences, University College London, London, UK.
[6]Scripps Institution of Oceanography, University of California San Diego, CA, USA.
[7]Instituto Mexicano del Petroleo, Gustavo Adolfo Madero, Mexico.

Key Points:

- We have modeled FORC diagrams for single-domain and single-vortex sized magnetite for a range of particle sizes and morphologies
- Single-vortex particles display complex structures in the FORC distribution with multiple peaks and troughs
- The main peaks of the single-vortex FORC distributions have higher coercivities than the single-domain peak.

Corresponding author: Lesleis Nagy, `Lesleis.Nagy@liverpool.ac.uk`

Abstract

Micromagnetic modelling allows the systematic study of the effects of particle size and shape on the first-order reversal curve (FORC) magnetic hysteresis response for magnetite particles in the single-domain (SD) and pseudo-single domain (PSD) particle size range. The interpretation of FORCs, though widely used, has been highly subjective. Here, we use micromagnetics to model randomly oriented distributions of particles to allow more physically meaningful interpretations. We show that one commonly found type of PSD particle – namely single vortex (SV) particles – has far more complex signals than SD particles, with multiple peaks and troughs in the FORC distribution, where the peaks have higher switching fields for larger SV particles. Particles in the SD to SV transition zone have the lowest switching fields. Symmetrical and prolate particles display similar behavior, with distinctive peaks forming near the vertical axis of the FORC diagram. In contrast, highly oblate particles produce 'butterfly' structures, suggesting that these are potentially diagnostic of particle morphology. We also consider FORC diagrams for distributions of particle sizes and shapes and produce an online application that users can use to build their own FORC distributions. There is good agreement between the model predictions for distributions of particle sizes and shapes, and the published experimental literature.

Plain Language Summary

In Earth, planetary and environmental sciences, magnetic methods are often used to rapidly measure the properties of rocks, sediments, meteorites, and soils. These magnetic properties can be proxies for environmental change or indicators of magnetic recording fidelity. The magnetic properties are dependent on the magnetic mineralogy and particle size and shape of the minerals within a sample. There is no single measurement that provides a unique interpretation; instead, a range of methods are applied, one of which is magnetic hysteresis analysis. First-order reversal curves (FORCs) are an advanced type of hysteresis analysis, and the FORC response of a minerals depends on magnetic domain state, which is strongly controlled by both the size and shape of a particle. We understand the FORC response of very big ($>$ 1000 nm) and very small particles ($<$100 nm), but interpretation for particles in between, the so called pseudo-single domain (PSD) state, has remained elusive. This is a problem as the magnetic signature of many rocks is dominated by PSD signals. In this paper we use numerical micromagnetic modeling to systematically study the effect of particle size and shape on particles that support a particular type of PSD FORC response – the single-vortex.

1 Introduction

In many geological and environmental studies it is important to be able to quantify the magnetic mineralogy including size and shape within samples. To do this, a range of methods are typically employed including first-order reversal curve (FORC) analysis. FORC diagrams are a type of detailed hysteresis measurement routinely used since their introduction to the rock and paleomagnetic community nearly 25 years ago (Pike et al., 1999; Roberts et al., 2000).

FORC diagrams have the advantage over standard major-hysteresis-loop analysis, since they map out numerous domain-state switching events/transitions that are characteristic of distributions of individual particles in the sample. FORC diagrams therefore provide an accumulation of hysteresis data from which to isolate and identify populations of magnetic domain states within typical natural samples (Egli, 2021; Roberts et al., 2022). For example, Rowan and Roberts (2005) used FORC analysis to identify greigite in paleomagnetically compromised New Zealand mudstones, which major-loop hysteresis failed to identify.

Many papers describe the construction of FORC diagrams (e.g., Pike & Fernandez, 1999; Pike et al., 1999; Roberts et al., 2000), however, we briefly outline how they are created and interpreted to give the background that we will draw on later in our discussion. FORC diagrams are generated from a series of first-order transition (reversal) curves (Mayergoyz, 1986), whereby the magnetization of a sample is first saturated in a field $B_{\rm sat}$ and thereafter the field is reduced to a reversal-field value $B_{\rm r}$ (Figure 1a). A first-order reversal curve is produced by measuring the sample's magnetization as the field is swept (from say $B_{\rm r}^i$) back up to saturation (black arrow in Figure 1a (right), when $i = 4$). A series of such reversal curves (from $i = 1, \cdots, n$) is produced as reversal-field values are successively chosen so that they approach negative saturation. We may then plot the magnetization against B and $B_{\rm r}$ field values (Figure 1b) where the main diagonal of the resulting triangle corresponds to the major hysteresis loop (blue curve in Figure 1a). It is common to plot values of magnetization directly and FORC diagrams are distribution density plots of the mixed second-order partial derivatives of the magnetization with respect to B and $B_{\rm r}$, given by

$$\rho(B_{\rm r}, B) \equiv -\frac{\partial^2 M(B_{\rm r}, B)}{\partial B_{\rm r} \partial B}. \tag{1}$$

FORC diagrams are typically plotted in field space ($B_{\rm c}$, $B_{\rm u}$), which geometrically corresponds to a rotation of the FORC diagram by 45° counter-clockwise (Figure 1c). $B_{\rm c}$ and $B_{\rm u}$ are:

$$B_{\rm c} \equiv (B - B_{\rm r})/2, \tag{2}$$

$$B_{\rm u} \equiv (B + B_{\rm r})/2. \tag{3}$$

As a first approximation, B_c is often taken as an approximation for the samples' coercivity distribution, and B_u correspond to magnetic interaction field values (Muxworthy & Williams, 2005). Although only strictly true for single domain (SD) particles, it remains useful convention for describing FORC diagrams.

A clearer understanding of ρ is obtained by considering the mixed derivative in Equation 1 in two parts. The first is the derivative $\partial M/\partial B$, which yields a peak whenever the magnetization changes rapidly, e.g., when a domain state changes from B^{i-1} to B^i for a switching field B^i. As the applied field B is swept from B_r to saturation at B_{sat}, M increases monotonically for SD and SV domain states if no thermal relaxation occurs, and so $\partial M/\partial B$ is positive; however the steepness of this curve changes as FORCs are taken from neighboring reversal-field values, i.e., when we consider the $\partial M/\partial B_r$ component of ρ. When we take the negative derivative of $\partial M/\partial B$ with respect to the reversal-field values, we are looking at the rate of change of the tangents of the FORC curves within the same neighborhood.

Whenever neighboring FORC curves are far apart at lower fields and converge together at higher fields (Figure 1a inset i), the value for ρ is positive and plots as red within our color scheme on the FORC diagram with larger changes in the local FORC gradients resulting in a deeper shade of red. On the other hand, when FORCs diverge over a region, ρ is negative (Figure 1a inset iii) and plots blue on our FORC diagrams, again deeper shades of blue correspond to greater divergence in neighboring FORCs. Finally, if there is no change, i.e., FORCs are parallel, then $\rho = 0$ and plots white (Figure 1a inset ii).

Key to interpreting FORC diagrams is understanding the response of different magnetic domain states; a magnetic domain-state depends on mineralogy and importantly on particle size and morphology, as well as other parameters like temperature and pressure. There are essentially four types of domain state, each with its own magnetic signature. Small magnetic particles are uniformly magnetized and are termed single domain (SD), with sizes $\lesssim$ 100 nm for equant magnetite (Kittel, 1949); the exact threshold sizes depend on geometry, temperature and stress levels in addition to size (Nagy et al., 2019a). Very small SD particles are thermally unstable at room temperature ($\sim$30 nm for magnetite), and are said to be superparamagnetic (SP) (Bean & Livingston, 1959), because they maintain equilibrium with the external magnetic field. The magnetization in large magnetic particles ($\gtrsim$10000 nm for magnetite) breaks up into areas of uniform magnetization separated by domain walls (multidomain, MD) (Nagy et al., 2019b). The intermediate particle size, i.e., $\sim$100–10000 nm for equant magnetite, experimentally displays behavior in some ways similar to that of SD particles, even though the particles are magnetically non-uniform and may even, at the upper end of this size range, have domain walls (MD). Particles in this region are often

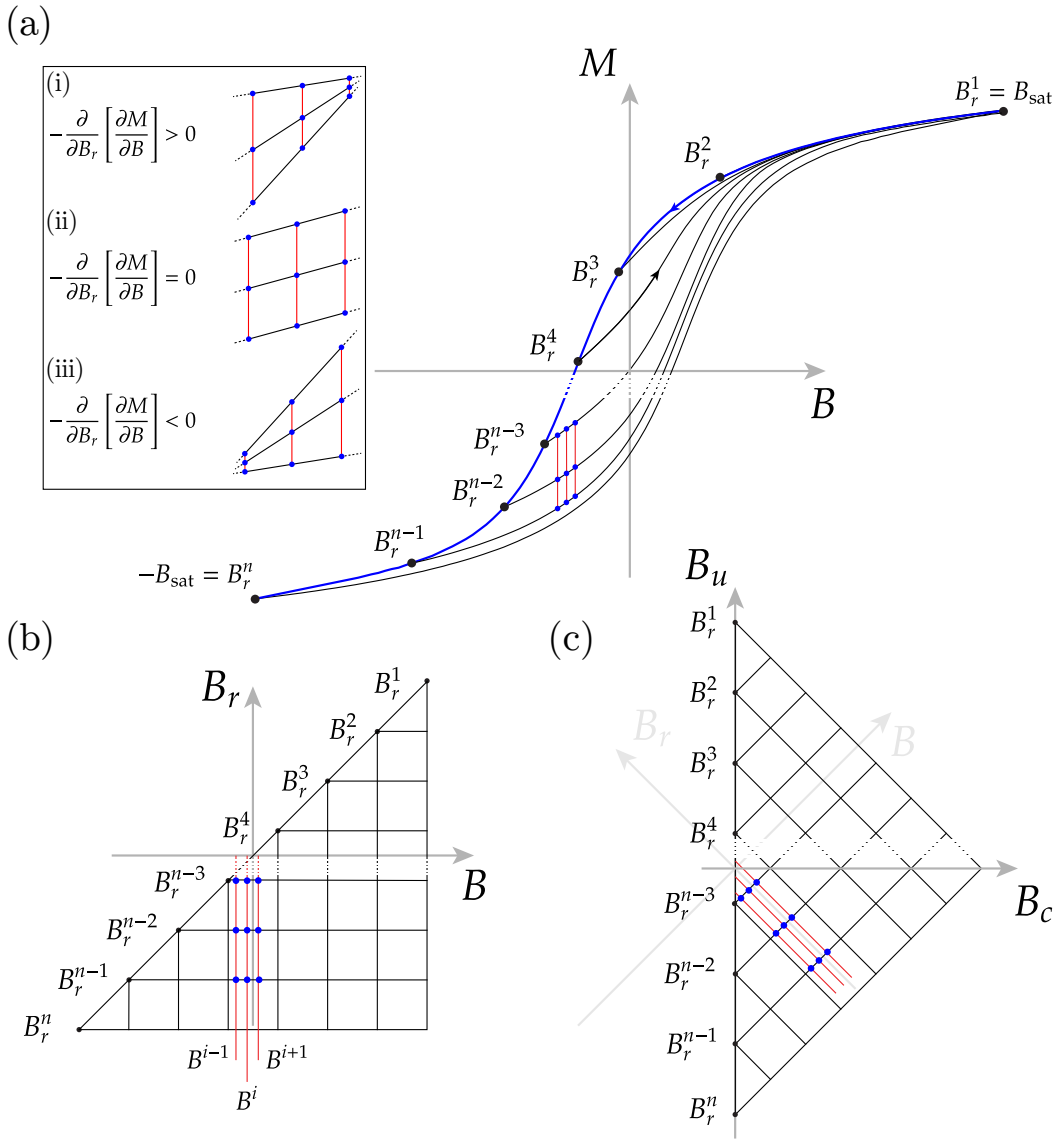

Figure 1. Construction of a FORC diagram. (a) In the experimental process shown, a sample is placed in a saturating field B_{sat}. The field is then reduced to a value of B_r^i $(i = 1, \cdots, n)$ and measurements of the magnetization, M, are made as the field is swept back up to saturation. This process produces a single first-order reversal curve (FORC). A series of FORCs are produced as B_r^i is reduced toward negative saturation. (b) The negative second-order partial derivative of the magnetization with respect to B_r and B (Equation 1) is plotted over the triangular domain of the reversal field (B_r) and the applied field (B), where the blue dots and red lines shown in the hysteresis loop stack in (a) corresponds to the blue dots in (b) and (c).

termed pseudo-SD (PSD) (Stacey, 1962). Despite decades of effort, beginning with the work of Enkin and Williams (1994), the controls on the stability (or instability) of so-called PSD particles have remained elusive.

The contributions of SP, SD and MD particles to FORC diagrams are well understood (Roberts et al., 2000, 2014, 2022), however, the contribution of PSD particles is less so. This is a problem, as PSD particles commonly dominate the magnetic signal of natural systems both in terms of abundance and paleomagnetic recording (Roberts et al., 2017; Nagy et al., 2019a). Historically, the reason for this poor understanding is twofold: (1) PSD particles display highly non-linear magnetic structures and behavior, and (2) they are also small and experimentally challenging to work with. However, our understanding of PSD particles has improved in the last ∼25 years through magnetic imaging techniques (Dunin-Borkowski et al., 1998; Almeida et al., 2014) and numerical micromagnetic modeling (Williams & Dunlop, 1989), which have shown that smaller PSD particles ($\lesssim$ 1000 nm for equant magnetite) typically display single-vortex (SV) structures. SV domain states have particular paleomagnetic importance because of their high remanence values and stabilities (Nagy et al., 2017). In the rest of this paper, we refer to SV particles since this is the primary type of PSD domain state observed in our micromagnetic models.

Even with our modern understanding of SV particles, the question remains: how do SV structures contribute to a FORC diagram? There have been several attempts to address this over the years both experimentally and theoretically. Experimental approaches have been hampered by the difficulty in producing measurable samples of near-identical non-interacting magnetic particles in this size range, and in the difficulty in producing sufficient samples that systematically describe a wide range of particle morphologies and sizes (e.g., Pike & Fernandez, 1999; Muxworthy et al., 2006; Dumas et al., 2007; Krása et al., 2011b; Chiba et al., 2020). There have been both phenomenological (Pike & Fernandez, 1999) and numerical (e.g., Carvallo et al., 2003; Lascu et al., 2018; Valdez-Grijalva et al., 2018) attempts to understand the FORC signature of SV particles. The FORC simulations of Carvallo et al. (2003) were limited computationally, whilst the models of Lascu et al. (2018) were only for very complex particle morphologies found in obsidian, and those of Valdez-Grijalva et al. (2018) for symmetric truncated-octahedral particles. There are still clear gaps in our understanding of the FORC response of SV particles.

In this paper we present a comprehensive and systematic suite of numerical models for mono-dispertions as well as distributions of randomly orientated prolate and oblate particles, with particle sizes between 40 to 195 nm (equivalent spherical-volume diameter, ESVD). We consider aspect ratios (AR) for the prolate (AR $>$ 1.0) and oblate (AR $<$ 1.0) magnetite particles at room temperature. Initially we consider populations of identical randomly ori-

entated particles, then later in the paper we consider distributions of particles with varying sizes and aspect ratio. We provide and describe a python code package (Synth-FORC), available at: `https://synth-forc.earthref.org/`, which can be used online or downloaded, for users to forward model their own FORC responses of distributions of SD and SV magnetite particles.

2 Methods

We have modeled FORCs for truncated-octahedral magnetite particles at room temperature for a range of sizes between 40 and 195 nm ESVD and for a range of aspect ratios (AR) for both prolate and oblate particles (AR between 0.125 and 6.0) using the SIMPLEFORC function of the micromagnetic algorithm MERRILL, version 1.4.6 (O Conbhuí et al., 2018). MERRILL uses tetrahedral-element meshes, which were generated using the meshing package Coreform Cubit (Coreform LLC, 2017). In the models, it is desirable to have the maximum mesh size no greater than the material's exchange length, which for magnetite is 9 nm (all our model geometries were meshed at 8 nm).

SIMPLEFORC first computes and saves the domain states along the upper branch of a hysteresis loop, which are subsequently used as the initial states for each reversal curve to saturation, forming a FORC dataset at regular field steps (Roberts et al., 2022). We made both 'low-resolution' FORC simulations with a field step size of 4 mT, and 'high-resolution' simulations with a step size of 1 mT. In our solutions no qualitative difference could be seen between the FORC diagrams computed at the different resolutions. We simulated the FORCs using a maximum field of 200 mT, and processed the FORC diagrams using the 'relaxed fit' algorithm (Roberts et al., 2014) written by Valdez-Grijalva et al. (2018). All models we present use a smoothing factor of three.

3 Simulated FORCs diagrams for random distributions

We outline the micromagnetic solutions for equant, prolate and oblate truncated-octahedral particles of magnetite. To simulate random distributions for each particle size and AR, we simulated FORC diagrams for 29 points evenly distributed over an octant of a sphere. Over all particle geometries, a total of 737 FORC diagrams were simulated, computed over several months. In the following analysis of domain state changes during FORC measurements, we attempt to identify the principle changes associated with features on the FORC diagrams. However, in any random distribution of particles, even for a mono-dispersion, more than one type of domain state change may contribute to a particular positive or negative peak in the FORC diagram. This is caused by differences in relative orientation between applied field and particle shape or magnetocrystalline anisotropy axes. To illustrate this we

have produced a series of videos (supplementary files equidimensional.mp4, prolate.mp4 and oblate.mp4) that follow the changing domain states in 20 identical particles, but with different orientations to the applied field. At each measurement point the domain states are shown, along with their corresponding point on the FORC diagrams. These videos provide a more comprehensive illustration of the main domain state changes described below.

3.1 Equant truncated-octahedral particles of magnetite

For equant particles, simulated FORC diagrams display a progression in behavior as the particle size increases from 45 nm ESVD through to 195 nm ESVD (Figure 2). The 45 nm particles are SD, switch coherently, and yield isolated contours as expected (Figure 2a). The FORC diagrams consist of a positive peak at B_c ~15 mT, with a negative peak just beneath it along the -B_u axis. This is similar to the predictions of truncated-octahedral particles of SD greigite (Valdez-Grijalva et al., 2018), although the peak B_c is lower for magnetite.

As the particle size increases there is almost no change in FORC distribution until 85 nm ESVD (Figure 2b), where a SV nucleates in the zero-field state with the vortex core aligned along the hard-axis like particles in the Low-Stability Zone (LSZ) observed by Nagy et al. (2017). This leads to a drop in the coercivity, and the main positive peak in the FORC distribution plots closer to the origin. On increasing the particle size to 105 nm ESVD, the FORC diagram changes to a more complex structure (Figure 2c). This corresponds to the remanence-state SV core aligning along one of the magnetocrystalline easy-axis of magnetite (Nagy et al., 2017). The FORC distribution now consists of a main positive peak at B_c ~40 mT, with a negative peak just below it, along with four positive peaks that plot along the B_u axis. There are two peaks in the $+B_u$ pane, mirrored by two peaks in the $-B_u$ pane; we term these four peaks the 'vertical near-axis peaks' (VNAP). VNAPs correspond to the behavior reported by Valdez-Grijalva et al. (2018); however, their diagrams do not extend far enough in the $+B_u$ direction, hiding some of the peaks on the B_u axis. On increasing the particle size to 195 nm ESVD (Figure 2d), all the peaks observed on the 105 nm simulation (Figure 2c) 'spread out' from the origin, i.e., the main peak moves from to ~40 mT to ~80 mT. In many of the figures, mottled textures due to minor negative peaks, are observed that spread downward and to the right from the minimum positive peak. These noisy tails are often seen in experimental FORCs and appear also in our models. The cause in both cases is the same, and are due to slightly different switching fields observed across multiple reversal curves (Moreno-Ortega et al., 2022).

The positive peak located on the B_c axis corresponds to vortex-core reversal (Figure 2d), which usually occurs as a rotation of vortex core though the hard anisotropy axis, towards the direction of the applied field (see supplementary material). This is a direct analogy

to SD domain state coherent rotation, and is a process we have previously described as structure-coherent rotation (Nagy et al., 2019b). The two VNAPs further away from the B_c axis correspond to the gradual transformation between a flower state (FS) and SD state; the degree of flowering increases as the applied field is reduced from saturating values (Figure 2d). Specifically, the $+B_u$ VNAP furthest from the B_c axis is due to de-nucleation of a SD state and formation of a flower state, while the mirrored $-B_u$ VNAP is due to nucleation of a FS from SD. The other two VNAPs closer to the B_c axis are due to transformation between a twisted flower state and an SV state (videos available at Nagy et al., 2023). The VNAPs appear close to the B_u axis because they describe a process that is locally reversible.

.

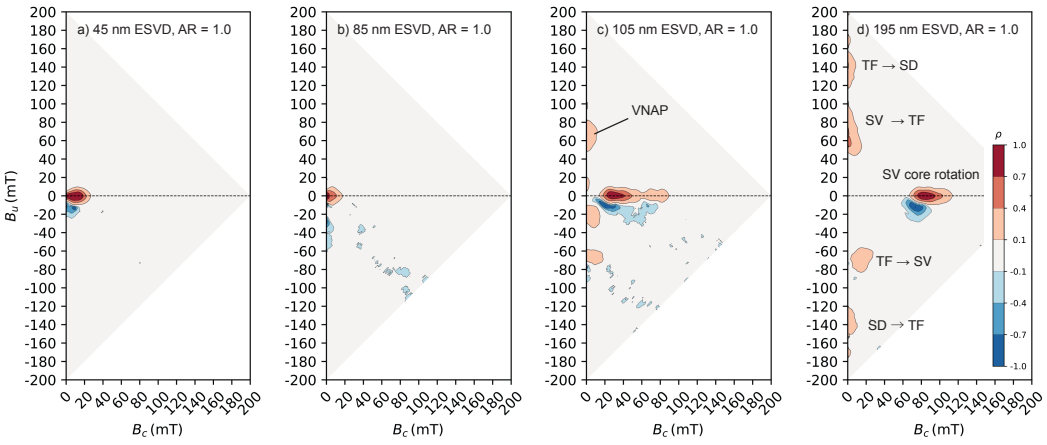

Figure 2. Simulated FORC diagrams for random-distributions of equant (AR = 1.0) truncated-octahedral magnetite particles of: a) 45 nm ESVD, b) 85 nm ESVD, c) 105 nm ESVD and d) 195 nm ESVD. In c) a VNAP is highlighted. In d) the origins of the peaks due to nucleation of a single domain (SD), twisted vortex (TF) domain states as well as SV core rotation toward and away from the applied field are labeled. The maximum applied field was 200 mT, and the step size in the simulation was 4 mT. For AR = 1.0, the truncated octahedral diameter is approximately equal to the ESVD.

3.2 Prolate truncated-octahedral particles of magnetite

We consider the effect of increasing AR up to 6.0 for truncated-octahedral magnetite particles for a range of sizes between 45 and 195 nm ESVD (Figure 3). For small elongations, i.e., < 1.25, the cubic magnetocrystalline anisotropy dominates, and the behavior is close to that of the symmetrical particles, i.e., AR = 1.0 (Figure 2). As AR increases, e.g., AR 1.5, the smallest particles, which are SD, i.e., 45 nm ESVD (Figure 3a), display FORC

diagrams typical for uniaxial SD particles, i.e., a positive main peak on the B_c axis, with a corresponding negative peak on the B_u axis (Muxworthy et al., 2004; Newell, 2005). This corresponds to the SD domain state switching towards the positive and negative field directions respectively at B_c ∼40 mT . The position of the main peak on the B_c axis is higher than for the case in which AR = 1 (Figure 2a), reflecting the increased SD coercivity with elongation. As the particle size increases, the trends follow that observed for AR = 1.0, that is, the main peak decreases at 105 nm ESVD, i.e., the LSZ (Figure 3b), before increasing to B_c ∼55 mT at 195 nm ESVD.

As AR increases, e.g., AR = 2.5 (Figures 3d-f), the position of the main peak on the B_c axis increases for SD particles, e.g., for 45 nm B_c ∼70 mT, as the relative absolute anisotropy increases. Also as AR increases, the SD to SV transition size also increases (Muxworthy & Williams, 2006). This causes the trends observed for the symmetric particles, to occur at relatively larger particle sizes: the main peaks along the central ridge decrease to B_c ∼20 mT at 145 nm, before increasing to B_c ∼45 mT at 195 nm ESVD. The FORC diagram for the 195 nm ESVD particle (Figure 3f), displays a series of negative and positive peaks (a 'NPNP' structure) running at a 45°angle from the B_u axis. NPNP structures have previously been suggested as being indicative of SV structures (Zhao et al., 2017; Valdez-Grijalva et al., 2018).

3.3 Oblate truncated-octahedral particles of magnetite

Oblate particles show similar trends with particle size as the prolate particles (Figures 3 and 4). For the nearly equant oblate particles, the trends are very similar to those of the equant particles (Figure 2), i.e., as the particle size increases, SD particles transition to hard-axis aligned vortex structures, which decreases the main peak position on the B_c axis. On further increase of the particle size, the main peak shifts to the right along the B_c axis and four mirrored VNAP features appear (cf., Figure 4a-c).

As AR is further decreased to AR ∼0.5, compared to the more equant particles, the trends are subtly different (Figure 4d-i): first, the transition from SD to SV is at larger particle sizes, similar to the prolate particles, and second, the VNAP structures form gradually over several particle sizes and are not initially on the axis. These differences are caused by the stronger planar anisotropy of the oblate particles, which encourages the spontaneous formation of SV states from the saturated SD states as the field is reduced. Similarly the positive lobe below the B_c axis corresponds to nucleation of the SV state (Dumas et al., 2007; Moreno-Ortega et al., 2022). However, nucleation of the SV state does not occur directly from SD, but via an inhomogeneous magnetic structure where there is some flowering of the surface magnetization together with planar rotation of the magnetization within the

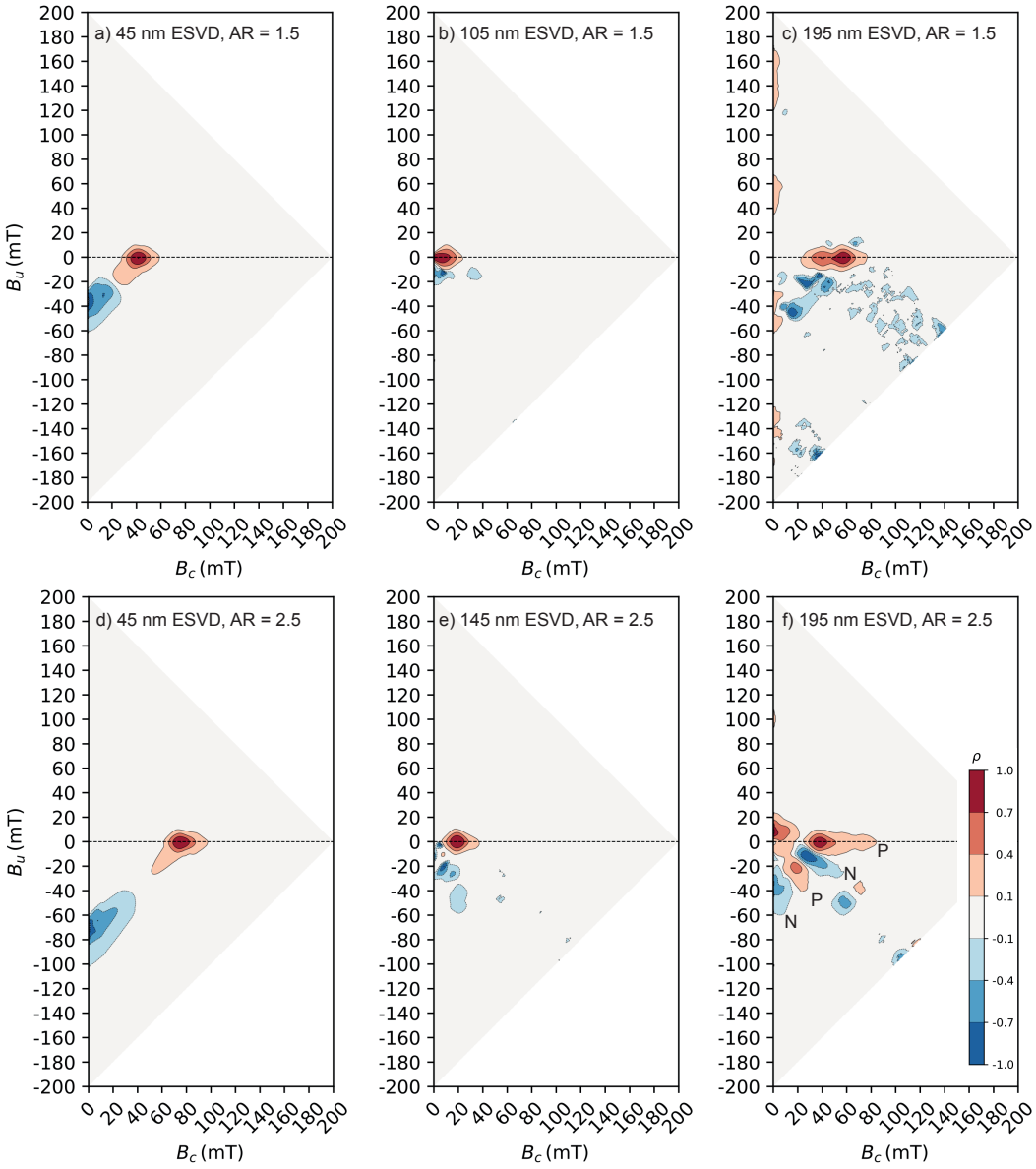

Figure 3. Simulated FORC diagrams for random-distributions of prolate truncated-octahedral magnetite particles of: a) 45 nm ESVD, AR = 1.5, maximum particle length (MGL) ∼ 59 nm b) 105 nm ESVD, AR = 1.5, MGL ∼ 137 nm c) 195 nm ESVD, AR = 1.5, MGL ∼ 255 nm d) 45 nm ESVD, AR = 2.5, MGL ∼ 83 nm e) 145 nm ESVD, AR = 2.5, MGL ∼ 267 nm, and f) 195 nm ESVD, AR = 2.5, MGL ∼ 359 nm. The maximum applied field was 200 mT, and the step size in the simulation was 1 mT.

particles. Such structures are are termed twisted flower (TF) states (Hertel & Kronmüller, 2002). The SD to TF transition is marked by the negative peak near the B_u axis at -40 mT, and the TF to SV transition indicated by the weak negative peak along the B_c axis (Figure 4e). The positive peaks collapse onto the B_u axis as the particle size increases to form true VNAPs (Figure 4f), and suggests that the SD to SV transition becomes a more reversible process at larger oblate particles sizes. These mirrored positive peaks either side of the B_c axis are often referred to as the butterfly FORC structure, highly indicative of SV states and commonly observed in high anisotropy monoclinic systems such as magnetite at low temperatures (Kobayashi et al., 2023) or high basal plane shape anisotropies of iron and cobalt platelets (Pike & Fernandez, 1999; Dumas et al., 2007; Chiba et al., 2020). For AR ∼0.25 (Figure 4i), the butterfly structures still exist, but for larger sizes, i.e., >185 nm, these disappear and NPNP or NPN structures arise. An atlas of all FORC diagrams we have modeled, as a function of particle size and shape is provided in the supplementary material and Nagy et al. (2023).

4 Discussion

We have shown that FORC distributions display a strong dependency on both particle size, shape and dominant anisotropy of magnetic particles, in agreement with previous studies (e.g., Carvallo et al., 2003; Valdez-Grijalva et al., 2018). Though compared to these previous studies the work here is more comprehensive; here we have used full-resolution models, better approximations for random orientation distributions and many more particle morphologies.

As particle size increases, and domain state switching changes from coherent SD switching to intermediate vortex states (Williams & Dunlop, 1995), the position of the peak coercivity initially decreases on the B_c axis (Figure 2). As the particle size further increases, e.g., 105 nm ESVD (Figure 2c), the peak shifts to higher values, higher than those observed for the smallest SD particles, e.g., 45 nm ESVD (Figure 2a). Increasing the particle size well above the SD-SV critical size, causes VNAPs to form, which reflect the continuous nature of the transformation from SD to SV. Increasing a particle's elongation in one direction (prolate) has two effects: (1) it causes the SD to vortex state critical size to increase, and (2) it causes the behavior to be controlled by a uniaxial-shape anisotropy (Butler & Banerjee, 1975; Muxworthy & Williams, 2006). The FORC diagrams reflect this, displaying behavior associated with uniaxial anisotropy (Muxworthy et al., 2004; Newell, 2005), and the particle size at which coherent switching stops is larger (Figure 3). However, the trends are the same as for the equant particles, i.e., the peak initially decreases on the B_c axis, before increasing for larger vortex particles with the formation of VNAPs. Our models demonstrate that for SV states in prolate particles, the FORC central ridge is formed by coherent rotation of

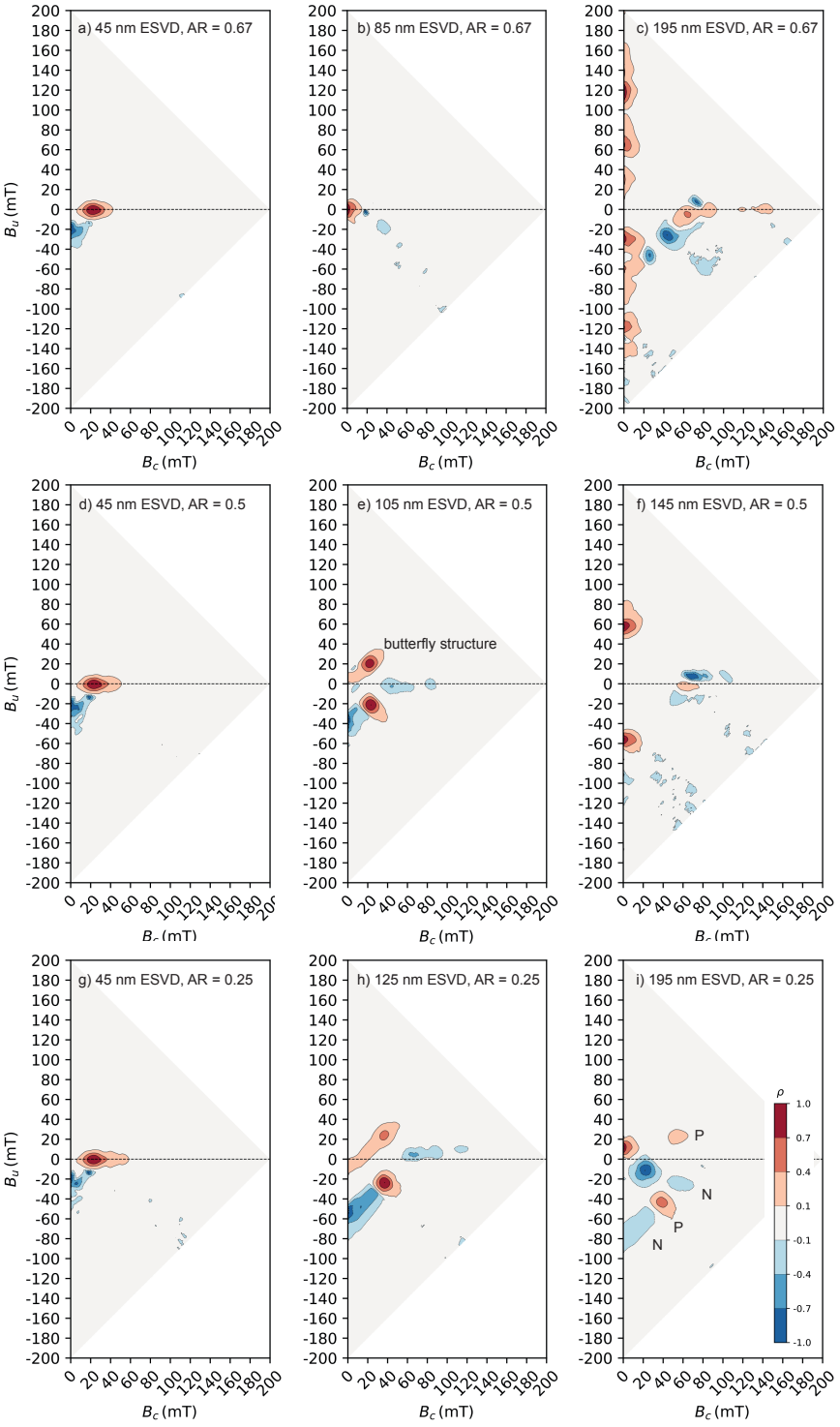

Figure 4. Simulated FORC diagrams for random-distributions of oblate truncated-octahedral magnetite particles of: a) 45 nm ESVD, AR = 0.67, MGL ∼ 51 nm, b) 85 nm ESVD, AR = 0.67, MGL ∼ 97 nm, c) 195 nm ESVD, AR = 0.67, MGL ∼ 222 nm, d) 45 nm ESVD, AR = 0.5, MGL ∼ 137 nm, e) 105 nm ESVD, AR = 0.5, MGL ∼ 132 nm, and f) 145 nm ESVD, AR = 0.5, MGL ∼ 182 nm, g) 45 nm ESVD, AR = 0.25, MGL ∼ 71 nm, h) 125 nm ESVD, AR = 0.25, MGL ∼ 198 nm, and i) 155 nm ESVD, AR =0.25, MGL ∼ 310 nm. The maximum applied field was 200 mT, and the step size in the simulation was 1 mT.

the vortex core, whose switching field is controlled by shape or crystalline anisotropy. In these particles, SD and SV states are therefore only distinguishable by the VNAPs peaks along the B_u axis caused by flower state and SV nucleation and denucleation. The oblate particles' FORC diagrams are more complex with more 'off-axis' features, e.g., the formation of butterfly structures, which are indicative of SV nucleation, but form only in the presence of high planar shape anisotropy in smaller SV particles. These SV signals collapse on to the vertical axis to form VNAPs in larger particle sizes for intermediate AR's (~ 0.5) (Figure 4).

For larger prolate and oblate particles with higher/lower ARs, NPN(P) structures form (Figures 3f and 4i). Such NPNP structures have been reported before for numerical models of FORC diagrams for vortex systems (e.g., Valdez-Grijalva et al., 2018), however, they are usually associated with induced-FORC (iFORC) diagrams, which are determined from transient and remanence FORC diagrams not modeled in this paper (Zhao et al., 2017; Tauxe et al., 2021; Roberts et al., 2022). These NPNP structures form when there are multiple metastable intermediate states during hysteresis, e.g., nucleation/de-nucleation of vortices, or flower structures or other metastable inhomogeneous magnetic domain states, switching between intermediate local energy minima (LEM; Carvallo et al., 2003; Valdez-Grijalva et al., 2018, 2020).

4.1 Comparison with experimental FORCs for mono-dispersions

There are only a few examples where FORC diagrams have been experimentally measured for (near) mono-dispersions of (near) non-interacting magnetite (Muxworthy et al., 2006; Krása et al., 2009, 2011b). To control the inter-particle spacing the samples are prepared by electron-beam lithography (EBL) (King et al., 1996). For direct comparison only, the studies of Krása et al. (2009, 2011b) overlap the particle size range calculated in this paper. The majority of the samples studied by Krása et al. (2009, 2011b) are arrays of plate like crystals, i.e., oblate. However, whilst most of these EBL samples are predicted to display SV behavior due to their particle volumes, they display mostly SD behavior (Krása et al., 2011a). A number of reasons have been suggested for this SD-like behavior: (1) EBL samples typically display magnetic behavior indicative of high levels of internal stress, which is thought to be due to the mismatch in crystal structure between the magnetite and the substrate, (2) it is thought that many of the EBL samples are polycrystalline, and (3) there is the possibility of surface oxidation of the samples, even though they are typically stored under alcohol after reduction. All these three processes produce more SD-like hysteretic behavior (Krása et al., 2009, 2011b, 2011a), as such we do not consider these EBL samples a 'good' comparison for this study. Nevertheless, for the near equidimensional sample DK0023 from (Krása et al., 2011b), our model predicts very similar results to their experimentally

measured FORCs. The tell-tail VNAPs indicative of DV domain states unfortunately fall outside the maximum B_u value in the experimental results.

Better examples of FORC diagrams measured using EBL samples are reported by Dumas et al. (2007) for iron. These EBL samples cover both the SD and SV particle size range, and consist of oblate particles with aspect ratios of ∼0.4. The general features observed for their 67 nm sample are replicated in our model in Figure 4f, i.e., the central positive peak on the B_c axis shadowed by negative peaks on either side, plus the two positive butterfly peaks, located symmetrically around the B_c axis. There is also the negative region on the B_u axis in the lower half of the diagram. This suggests that our model is accurately capturing the main features of SV behavior.

4.2 Distributions of particle-sizes and morphologies

In natural samples, mono-dispersions are rare, so we consider FORC diagrams for particle-size and morphology distributions of randomly oriented particles (Figure 5). This is similar to the approach of Valdez-Grijalva et al. (2018) for symmetric greigite. However, here we have systematically modeled a greater particle size range, plus we have included a wide range of aspect ratios; it is clear that particle morphology has a significant contribution to FORC distributions (*cf.* Figures 2–4).

We have used lognormal particle-size and morphology distributions to combine our FORC models (Figure 5). We consider two scenarios: a mean of 150 nm and one of 200 nm, both with particle morphology distributions with a mean AR of one (Figure 5). We truncate the distributions when we have no models to populate the distribution, e.g., a mean of 200 nm (Figure 5b) contains no models for particles $>$ 195 nm in size. The 150 nm case has a ridge from the origin along the B_c axis, whilst the 200 nm sample does not contain a ridge, it just has a peak at B_c ∼110 mT. The 200 nm distribution is similar to the 'true' SV structure (Figures 3c or 4c).

On initial inspection, it might appear that neither of these FORC diagrams match the typical measured 'PSD' FORC diagram (e.g., Roberts et al., 2014), however, this maybe because most natural systems have wider distributions of particle size than considered in our models. If we look at natural samples with quantified narrow particle size distributions, there is a strong similarity in behavior; for example, Lappe et al. (2011) studied dusty-olivine samples using off-axis electron holography to demonstrate that the iron particles in the samples were dominated by SV particles. The measured FORC diagram for these samples (Lappe et al., 2011), displays a strong similarity to Figure 5a, suggesting that our models accurately capture the main features of our true SV behavior.

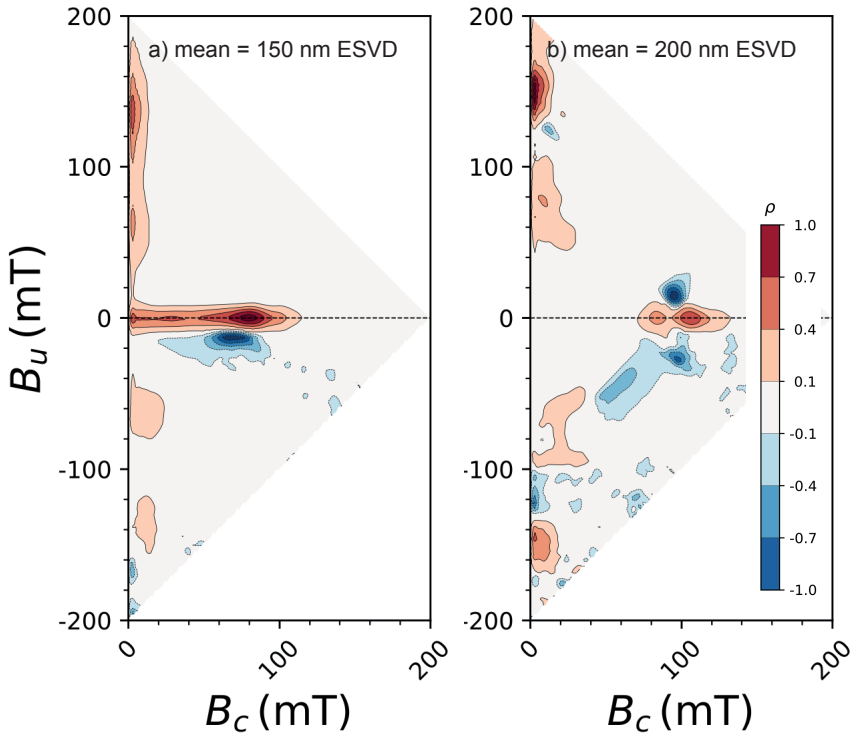

Figure 5. Simulated FORC diagrams for random-distributions of magnetite truncated-octahedral particles with lognormal distributions of both particle size and AR: a) mean particle size = 150 nm (variance, $\sigma^2 = 0.3$), mean AR = 1.2 with $\sigma^2 = 0.3$, and b) mean particle size = 200 nm ($\sigma^2 = 0.3$), mean AR = 1.0 ($\sigma^2 = 0.3$).

4.3 Synth-FORC

As part of the paper we have written the Synth-FORC (`https://synth-forc.earthref.org/`), which allows the user to forward model log-normal distributions of particles constructed from combining our results from particle mono-dispersions. The user can plot FORCs for their own particle distributions to produce diagrams similar to those in Figure 5. Currently the range of AR must lie between 0.125 and 6.0, and the particle sizes between 40 nm and 195 nm. Over time Synth-FORC will be updated with larger particle sizes, with the aim of eventually accounting for the complete SD and PSD particle size range.

5 Conclusions

We have made a systematic numerical study of the effect of particle size and shape on the FORC diagram response of SD and SV magnetite particles. We have shown that peak coercivities are higher for SV particles than SD particles, and vertical near-axis peaks (VNAPs)

are an indicator of SV behavior (Figure 2). FORC signals from SV particles can be elusive. SV particles contribute to the positive B_u region of the FORC diagram; we recommend that experimentalists routinely measure to high positive B_u values as this is currently not routine. Butterfly structures, which have been associated with SV behavior only appear in models for oblate particles just above the SD threshold (Figure 4) have also experimentally been observed for magnetite shells (Chiba et al., 2020). For larger SV particles, i.e., close to 195 nm, NPNP structures occur. These NPNP structures are indicative of multiple vortex nucleation/de-nucleation events. In samples with a distribution of particle sizes and shapes the FORCs become more complex still, although these complex FORCs have a distinctively different character from the simple SD or prolate SV patterns.

There is some experimental evidence from the literature to support these model findings (e.g., Dumas et al., 2007; Lappe et al., 2011). However, the number of studies on natural samples with an SV-only signal is thought to be limited.

6 Open Research

All results reported here were generated using the open source micromagnetic modeling code of O Conbhuí et al. (2018). Supplementary videos, input scripts and geometries used to construct the models in the paper are available at Nagy et al. (2023). Source code for MERRILL is available at `https://bitbucket.org/wynwilliams/merrill/` and is provided under a CC-BY-SA 4.0 International license.

Acknowledgments

L.N. acknowledges support of NERC grant NE/V014722/1. L.T., W.W. and L.N. acknowledge support of NSFGEO-NERC grant EAR1827263. G.A.P. acknowledge support from NERC grants NE/P017266/1 and NE/W006707/1. A.R.M. and W.W. acknowledge support from NERC grants NE/S001018/1 and NE/V001388/1. R.M acknowledges postdoctoral grant scheme of Conicet (Argentina).

References

Almeida, T. P., Kasama, T., Muxworthy, A. R., Williams, W., Nagy, L., Hansen, T. W., ... Dunin-Borkowski, R. E. (2014). Visualized effect of oxidation on magnetic recording fidelity in pseudo-single-domain magnetite particles. *Nature Communications*, *5*(1), 1–6. doi: 10.1038/ncomms6154

Bean, C. P., & Livingston, J. D. (1959). Superparamagnetism. *Journal of Applied Physics*, *30*(4), 120S-129S. doi: 10.1063/1.2185850

Butler, R. F., & Banerjee, S. K. (1975). Theoretical single-domain grain size range in

magnetite and titanomagnetite. *Journal of Geophysical Research*, *80*, 4049-4058. doi: 10.1029/JB080i029p04049

Carvallo, C., Muxworthy, A. R., Dunlop, D. J., & Williams, W. (2003). Micromagnetic modeling of first-order reversal curve (forc) diagrams for single-domain and pseudo-single-domain magnetite. *Earth and Planetary Science Letters*, *213*(3-4), 375-390. doi: 10.1016/S0012-821x(03)00320-0

Chiba, M., Kobayashi, S., Noguchi, K., Murakami, T., Szpunar, J. A., & Manjanna, J. (2020). Magnetic vortex formation in hollow fe3o4 submicron particles studied using first-order reversal curves. *Journal of Magnetism and Magnetic Materials*, *512*, 167012. doi: 10.1016/j.jmmm.2020.167012

Coreform LLC. (2017). *Coreform Cubit, v16.4 (64-Bit).* Retrieved from `https://coreform.com`

Dumas, R. K., Li, C.-P., Roshchin, I. V., Schuller, I. K., & Liu, K. (2007, Apr). Magnetic fingerprints of sub-100 nm fe dots. *Physical Review B*, *75*, 134405. doi: 10.1103/PhysRevB.75.134405

Dunin-Borkowski, R. E., McCartney, M. R., Frankel, R. B., Bazylinski, D. A., Posfai, M., & Buseck, P. R. (1998). Magnetic microstructure of magnetotactic bacteria by electron holography. *Science*, *282*(5395), 1868-1870. doi: 10.1126/science.282.5395.1868

Egli, R. (2021). Magnetic characterization of geologic materials with first-order reversal curves [Book Section]. In V. Franco & B. Dodrill (Eds.), *Magnetic measurement techniques for materials characterization* (p. 455-604). Cham: Springer International Publishing. doi: 10.1007/978-3-030-70443-8_17

Enkin, R. J., & Williams, W. (1994). Three-dimensional micromagnetic analysis of stability in fine magnetic grains. *Journal of Geophysical Research*, *99*(B1), 611-618. doi: 10.1029/93JB02637

Hertel, R., & Kronmüller, H. (2002). Finite element calculations on the single-domain limit of a ferromagnetic cube—a solution to mag standard problem no. 3. *Journal of Magnetism and Magnetic Materials*, *238*(2), 185-199. doi: 10.1016/S0304-8853(01)00876-9

King, J., Williams, W., Wilkinson, C. D. W., McVitie, S., & Chapman, J. N. (1996). Magnetic properties of magnetite arrays produced by the method of electron lithography. *Geophysical Research Letters*, *23*(20), 2847-2850. doi: 10.1029/96GL01371

Kittel, C. (1949). Physical theory of ferromagnetic domains. *Reviews of Modern Physics*, *21*(4), 541. doi: 10.1103/RevModPhys.21.541

Kobayashi, S., Nomura, E., Noda, C., Manjanna, J., Jargalan, N., Uyanga, E., ... Sangaa, D. (2023). Magnetization process of cubic fe3o4 submicron particles: First-order reversal curves and neutron diffraction studies. *Journal of Magnetism and Magnetic*

Materials. doi: 10.1016/j.jmmm.2023.171509

Krása, D., Muxworthy, A., & Williams, W. (2011a). Additional FORC diagrams from 'Room- and low-temperature magnetic properties of two-dimensional magnetite particle arrays'. [dataset]. *Zenodo*. doi: 10.5281/zenodo.7958372

Krása, D., Muxworthy, A., & Williams, W. (2011b). Room- and low-temperature magnetic properties of two-dimensional magnetite particle arrays. *Geophysical Journal International*, *185*, 167–180. doi: 10.1111/j.1365-246X.2011.04956.x

Krása, D., Wilkinson, C., Gadegaard, N., Kong, X., Zhou, H., Roberts, A., ... Williams, W. (2009). Nanofabrication of two-dimensional arrays of magnetite particles for fundamental rock magnetic studies. *Journal of Geophysics Research-Solid Earth*, *114*. doi: 10.1029/2008JB006017

Lappe, S., Church, N. S., Kasama, T., Fanta, A. B. D., Bromiley, G., Dunin-Borkowski, R. E., ... Harrison, R. J. (2011). Mineral magnetism of dusty olivine: A credible recorder of pre-accretionary remanence. *Geochemistry Geophysics Geosystems*, *12*. doi: 10.1029/2011gc003811

Lascu, I., Einsle, J. F., Ball, M. R., & Harrison, R. J. (2018). The vortex state in geologic materials: A micromagnetic perspective. *Journal of Geophysical Research-Solid Earth*, *123*(9), 7285-7304. doi: 10.1029/2018jb015909

Mayergoyz, I. (1986). Mathematical models of hysteresis. *IEEE Transactions on Magnetics*, *22*(5), 603-608. doi: 10.1109/TMAG.1986.1064347

Moreno-Ortega, R., Williams, W., Muxworthy, A., Paterson, G., & Heslop, D. (2022). The meaning of maxima and minima in first order reversal curves: Determining the interaction between species in a sample. *Journal of Magnetism and Magnetic Materials*, *564*, 170042. doi: 10.1016/j.jmmm.2022.170042

Muxworthy, A. R., Heslop, D., & Williams, W. (2004). Influence of magnetostatic interactions on first-order-reversal-curve (FORC) diagrams: a micromagnetic approach. *Geophysical Journal International*, *158*(3), 888-897. doi: 10.1111/j.1365-246X.2004.02358.x

Muxworthy, A. R., King, J., & Odling, N. (2006). Magnetic hysteresis properties of interacting and noninteracting micron-sized magnetite produced by electron beam lithography. *Geochemistry Geophysics Geosystems*, *7*(Q07009). doi: 10.1029/2006GC001309

Muxworthy, A. R., & Williams, W. (2005). Magnetostatic interaction fields in first-order-reversal-curve diagrams. *Journal of Applied Physics*, *97*(6). doi: 10.1063/1.1861518

Muxworthy, A. R., & Williams, W. (2006). Critical single-domain/multidomain grain sizes in noninteracting and interacting elongated magnetite particles: Implications for magnetosomes. *Journal of Geophysical Research-Solid Earth*, *111*(B12). doi: 10.1029/2006jb004588

Nagy, L., Moreno Ortega, R., Muxworthy, A. R., Williams, W., Paterson, G. A., Tauxe, L., & Valdez-Grijalva, M. A. (2023). Micromagnetic determination of the forc response of paleomagnetically significant magnetite assemblages [dataset]. *Zenodo*. doi: 10.5281/XXXXX

Nagy, L., Williams, W., Muxworthy, A. R., Fabian, K., Almeida, T. P., Ó Conbhuí, P., & Shcherbakov, V. P. (2017). Stability of equidimensional pseudo-single-domain magnetite over billion-year timescales. *Proceedings of the National Academy of Sciences of the United States of America*, *114*(39), 10356-10360. doi: 10.1073/pnas.1708344114

Nagy, L., Williams, W., Tauxe, L., & Muxworthy, A. R. (2019b). From nano to micro: Evolution of magnetic domain structures in multidomain magnetite. *Geochemistry Geophysics Geosystems*, *20*(6), 2907 – 2918. doi: 10.1029/2019gc008319

Nagy, L., Williams, W., Tauxe, L., Muxworthy, A. R., & Ferreira, I. (2019a). Thermomagnetic recording fidelity of nanometer-sized iron and implications for planetary magnetism. *Proceedings of the National Academy of Sciences of the United States of America*, *116*(6), 1984-1991. doi: 10.1073/pnas.1810797116

Newell, A. J. (2005). A high-precision model of first-order reversal curve (forc) functions for single-domain ferromagnets with uniaxial anisotropy. *Geochemistry Geophysics Geosystems*, *6*, Q05010. doi: 10.1029/2004GC000877

O Conbhuí, P., Williams, W., Fabian, K., Ridley, P., Nagy, L., & Muxworthy, A. R. (2018). Merrill: Micromagnetic earth related robust interpreted language laboratory. *Geochemistry Geophysics Geosystems*, *19*(4), 1080-1106. doi: 10.1002/2017gc007279

Pike, C. R., & Fernandez, A. (1999). An investigation of magnetic reversal in submicron-scale co dots using first order reversal curve diagrams. *Journal of Applied Physics*, *85*(9), 6668-6676. doi: 10.1063/1.370177

Pike, C. R., Roberts, A. P., & Verosub, K. L. (1999). Characterizing interactions in fine magnetic particle systems using first order reversal curves. *Journal of Applied Physics*, *85*(9), 6660-6667. doi: 10.1063/1.370176

Roberts, A. P., Almeida, T. P., Church, N. S., Harrison, R. J., Heslop, D., Li, Y. L., ... Zhao, X. (2017). Resolving the origin of pseudo-single domain magnetic behavior. *Journal of Geophysical Research-Solid Earth*, *122*(12), 9534-9558. doi: 10.1002/2017jb014860

Roberts, A. P., Heslop, D., Zhao, X., Oda, H., Egli, R., Harrison, R. J., ... Sato, T. (2022). Unlocking information about fine magnetic particle assemblages from first-order reversal curve diagrams: Recent advances. *Earth-Science Reviews*, *227*, 103950. doi: 10.1016/j.earscirev.2022.103950

Roberts, A. P., Heslop, D., Zhao, X., & Pike, C. R. (2014). Understanding fine magnetic particle systems through use of first-order reversal curve diagrams. *Reviews of Geophysics*, *52*(4), 557–602. doi: 10.1002/2014RG000462

Roberts, A. P., Pike, C., & Verosub, K. L. (2000). First-order reversal curve diagrams: A new tool for characterizing the magnetic properties of natural samples. *Journal of Geophysical Research*, *105*, 28461-28475. doi: 10.1029/2000JB900326

Rowan, C. J., & Roberts, A. P. (2005). Tectonic and geochronological implications of variably timed magnetizations carried by authigenic greigite in marine sediments from New Zealand. *Geology*, *33*(7), 553–556. doi: 10.1130/G21382.1

Stacey, F. D. (1962). A generalized theory of thermoremanence, covering the transition from single domain to multi-domain magnetic grains. *Philosophical Magazine*, *7*, 1887-1900. doi: 10.1080/14786436208213853

Tauxe, L., Santos, C., Cych, B., Zhao, X., Roberts, A., Nagy, L., & Williams, W. (2021). Understanding nonideal paleointensity recording in igneous rocks: Insights from aging experiments on lava samples and the causes and consequences of "fragile" curvature in Arai plots. *Geochemistry, Geophysics, Geosystems*, *22*(1), e2020GC009423. doi: 10.1029/2020GC009423

Valdez-Grijalva, M. A., Muxworthy, A. R., Williams, W., Ó Conbhuí, P., Nagy, L., Roberts, A. P., & Heslop, D. (2018). Magnetic vortex effects on first-order reversal curve (FORC) diagrams for greigite dispersions. *Earth and Planetary Science Letters*, *501*, 103-111. doi: 10.1016/j.epsl.2018.08.027

Valdez-Grijalva, M. A., Nagy, L., Muxworthy, A. R., Williams, W., Roberts, A. P., & Heslop, D. (2020). Micromagnetic simulations of first-order reversal curve (FORC) diagrams of framboidal greigite. *Geophysical Journal International*, *222*(2), 1126-1134. doi: 10.1093/gji/ggaa241

Williams, W., & Dunlop, D. J. (1989). Three-dimensional micromagnetic modelling of ferromagnetic domain structure. *Nature*, *337*(6208), 634–637. doi: 10.1038/337634a0

Williams, W., & Dunlop, D. J. (1995). Simulation of magnetic hysteresis in pseudo-single-domain grains of magnetite. *Journal of Geophysical Research*, *100*(B3), 3859-3871.

Zhao, X., Roberts, A. P., Heslop, D., Paterson, G. A., Li, Y., & Li, J. (2017). Magnetic domain state diagnosis using hysteresis reversal curves. *Journal of Geophysical Research-Solid Earth*, *122*(7), 4767-4789. doi: 10.1002/2016JB013683